Underground Natural Gas Microleakage Detection With Hyperspectral Imagery Based on Temporal Features and Ensemble Learning

Jinbao Jiang, Yingyang Pan, Kangning Li, Xinda Wang, and Wenxuan Zhang

***Abstract*—Microleakage in underground natural gas storage has serious impacts on the environment or public safety. Recent studies have shown that hyperspectral imagery can detect natural gas microleakage by spectral or spatial features of vegetation indirectly. However, the identification of natural gas microleakage based on hyperspectral imagery still suffers from the following problems: the spectral and spatial features of vegetation change in a complex way with increasing stress time; the effectiveness of ensemble classifiers in recognizing natural gas-stressed vegetation in hyperspectral imagery is unclear; and there is also a lack of studies on the spatial and temporal changes of vegetation stress in natural gas microleakage. Therefore, hyperspectral images of wheat, bean, and grass in different periods were collected. First, the spectral features were filtered using the Relief-F algorithm. The spatial texture features were extracted using the grayscale co-occurrence matrix. The temporal features were extracted using the bi-temporal band ratio. Then, an ensemble classification model fusing spectral, spatial, and temporal features was established. Finally, the natural gas microleakage information was extracted based on the minimum external circle, and the spatial-temporal changes of vegetation stress were analyzed. The results showed that the average stress radii of wheat, bean, and grass were 1.07, 0.83, and 0.86 m, respectively. The mean absolute localization error of natural gas microleakage points was less than 0.4 m. This study provides a theoretical basis and technical support for the future use of satellite hyperspectral detection of microleakage in underground gas storage reservoirs.**

***Index Terms*—Ensemble classification, feature fusion, hyperspectral imagery, natural gas microleakage.**

I. Introduction

NATURAL gas is widely used in various fields such as industrial fuels, electricity, and transportation [1], playing an increasingly important role in the global energy consumption system. Underground gas storage is very suitable for natural gas storage because of its advantages such as large storage capacity, high mobility, and low operating costs [2]. However, there is a risk of leakage from natural gas storage or underground pipelines due to factors such as the aging of pipelines, geological stress, or human damage [3]. Natural gas leakage will not only cause energy loss but also may cause serious environmental pollution [4], [5]. Under certain conditions, natural gas may also explode when mixed with air [6]. In addition, natural gas leakage could reduce the operational efficiency of gas storage and increase the cost of storing natural gas. In order to realize the safe and stable operation of underground gas storage, it is important to detect the underground gas leakage information timely and accurately.

Traditional detection methods focus on detecting natural gas leaks through changes in pipeline pressure, temperature, or flow rate [7]. However, the pressure changes caused when closing or opening the valve can cause false identification of leaks. In addition, this detection method is not ideal for detecting small leaks. Therefore, a more efficient and convenient detection method is needed. Natural gas is a low-quality hydrocarbon, and when a slight leakage occurs in an underground storage reservoir or pipeline, its migration path in the soil is generally vertical upward [8]. Therefore, it will compress the original soil air, making the vegetation roots in a low oxygen environment, affecting the normal growth and development of vegetation, thus causing changes in vegetation chlorophyll content and canopy reflectance [9], [10]. As a noncontact technology, hyperspectral image remote sensing can obtain real-time, rapid, and nondestructive information on surface vegetation changes, and can detect underground gas leakage nondestructively and indirectly [11], [12].

Many scholars in China and abroad have conducted studies related to the detection of natural gas or other hydrocarbon leakage using hyperspectral images. Van der Werff et al. [13] used two successive Hough transforms to extract spatial information from images and combined with spectral information to identify natural gas microleakage areas from hyperspectral imagery, which revealed surface vegetation stress ranging from 5 to 14 m in diameter and reduced false identification rates. Noomen et al. [14] combined spectral vegetation indices and spatial filters to detect anomalous vegetation caused by gas leakage in the field using Probe-1 hyperspectral imagery and found that the number of "false anomalies" was significantly reduced compared to that detected using spectral information. Male et al. [15] conducted a CO_2 microleakage stress field experiment in Montana, USA. Canopy hyperspectral and airborne

Manuscript received 21 July 2023; revised 30 September 2023; accepted 14 November 2023. Date of publication 22 November 2023; date of current version 8 December 2023. This work was supported by the National Natural Science Foundation of China under Grant 42271389 and Grant 41571412. *(Corresponding author: Kangning Li.)*

The authors are with the College of Geoscience and Surveying Engineering, China University of Mining and Technology-Beijing, Beijing 100083, China (e-mail: jjb@cumtb.edu.cn; cjpyynal@163.com; kangning@cumtb.edu.cn; wangxdrs@163.com; zhangwenxuan@student.cumtb.edu.cn).

Digital Object Identifier 10.1109/JSTARS.2023.3335289

hyperspectral images of the experimental area were collected. The spectral and spatial features were combined with the spectral angular mapping method for CO_2 microleakage point detection, and good results were achieved. Noomen et al. [16] used multitemporal HyMap hyperspectral imagery to detect the bioremediation status after microleakage of underground hydrocarbon transport pipelines, and used normalized vegetation indices to standardize the two-temporal images of 17 sampling sites for comparative analysis. The results showed a user detection accuracy of 71% over three years. Jiang et al. [17] constructed spectral index and color features based on hyperspectral images, and fused the two types of detection results using the shape detection algorithm and linear weighted fusion method, which can significantly improve the detection accuracy of natural gas microleakage points. Du et al [18] proposed that combining CNN and SAFY modeling methods can accurately detect natural gas leaks based on UAV hyperspectral images.

Although the use of hyperspectral imaging remote sensing is considered a promising method for detecting natural gas microleakage, the potential of this technology has not yet been fully realized. At present, most researchers focus on the spectral and spatial features of hyperspectral images, but do not study the temporal features of the images in depth. The spectral and spatial features of surface-stressed vegetation change with increasing stress time during natural gas microleakage. For the hyperspectral images with multiple time series, its advantage is mainly the ability to obtain temporal features that cannot be extracted from single-time phase images. Remote sensing images based on time-series features are widely used for land cover change [19], natural disaster monitoring [20], and biological stress identification [21]. However, the application in the field of natural gas microleakage stress identification is still insufficient. The main reasons are as follows: first, it is usually difficult to obtain hyperspectral images with multiple time series for the study area, and thus, cannot obtain its temporal features; second, there is a lack of methods to construct suitable temporal features of natural gas microleakage stress vegetation. Traditional methods for temporal phase feature analysis of images, such as principal component analysis, wavelet analysis, or Fourier analysis, which rely on the labeling of the change component of the ground object type [22], are a tedious process. In addition, the spectral characteristics of surface vegetation are highly dependent on the phenological stage of the vegetation [23]. In a single date scene, the spectral characteristics of vegetation have a weaker ability to respond to external stress and disturbance, and may fluctuate with phenological differences or environmental changes. Temporal spectral features allows stable access to vegetation phenology differences between temporal scenarios, thus characterizing the progressive development of internal and external symptoms caused by vegetation lesions while suppressing other confounding factors (e.g., soil background albedo and light effects) [24]. Therefore, it is necessary to design a fast and efficient method for temporal feature extraction.

In recent years, machine-learning algorithms have performed well in hyperspectral imaging classification and recognition applications, which can model high-dimensional data and adapt to multisource data fusion processing. Rumpf et al. [25] used nine vegetation indices related to physiological parameters as features for nondestructive identification of diseased and healthy sugar beet by support vector machine (SVM) with radial basis function as the core, with a classification accuracy of 97%. Tian et al. [26] used disease specific spectral features and machine-learning-based sequential floating forward selection to detect rice blast at different infection stages and showed classification accuracies higher than 65% and 80% for asymptomatic infection and early infection stages, respectively. In addition, it is difficult for a single classifier to maintain excellent performance for multiple classification scenarios all the time [27]. Compared to a single classifier, an ensemble classifier (EC) can achieve better classification results [28]. Yuan et al. [29] used three classifiers, SVM, PLS-DA, and SIMCA, to form an EC with an overall classification accuracy of 97.66% for pixel-level classification of healthy and moldy peanuts, all of which outperformed other individual classifiers. Yao et al. [30] developed the ensemble learning model for wetland vegetation mapping by superimposing Random Forest (RF), CatBoost, and XGBoost algorithms, and found that ensemble learning has better performance than using a single machine-learning model, with an overall accuracy between 77.02% and 92.27%.

The current hyperspectral image-based identification of natural gas microleakage stressed vegetation has the following problems:

1) existing studies mainly use the spectral features or spatial features of the images, but rarely consider the temporal features of the images in depth;
2) EC has stronger generalization ability and better classification performance than a single classifier, and has better stability in classification application of hyperspectral images, but it has not been applied in hyperspectral recognition classification of natural gas microleakage stressed vegetation;
3) lack of spatial and temporal analysis of vegetation stress under natural gas microleakage.

Therefore, this study collected the multitemporal hyperspectral imaging data of wheat, bean, and grass under the condition of simulating the microleakage of natural gas in the field. First, the spectral, spatial, and temporal features of hyperspectral images were extracted and fused. Then, EC was used to classify the natural gas microleakage stress vegetation, and a multifeature fusion stress vegetation identification model was constructed. Finally, the minimum external circle algorithm was used to extract the natural gas microleakage stress vegetation area and leak point location, and the spatial and temporal variation of the stress area range was analyzed.

II. Materials and Methods

A. Experimental Design

The experimental site was located in a farmland in Zhangziying Town, Daxing District, Beijing (39°39'2.56"N, 116°34'33.10"E). The experimental subjects included three types of surface vegetation: wheat, bean, and grass. Eight plots of 2.5 m × 2.5 m were set up for each vegetation, including four gas groups and four control groups, where the odd numbered

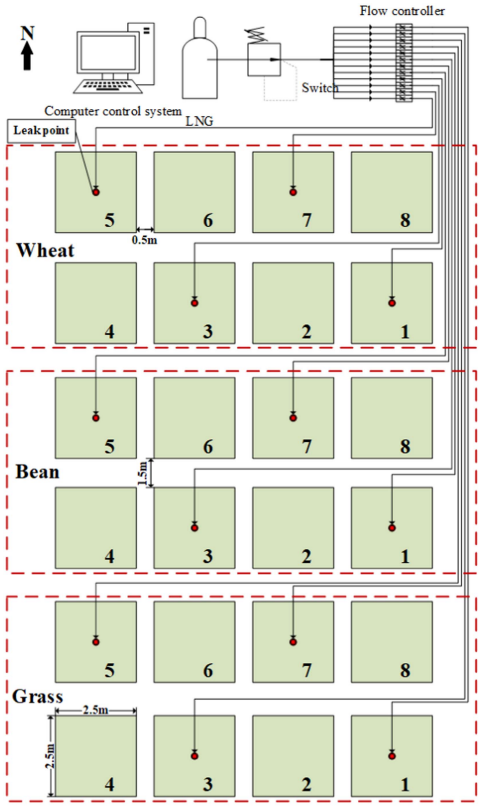

Fig. 1. Overview map of the field experiment.

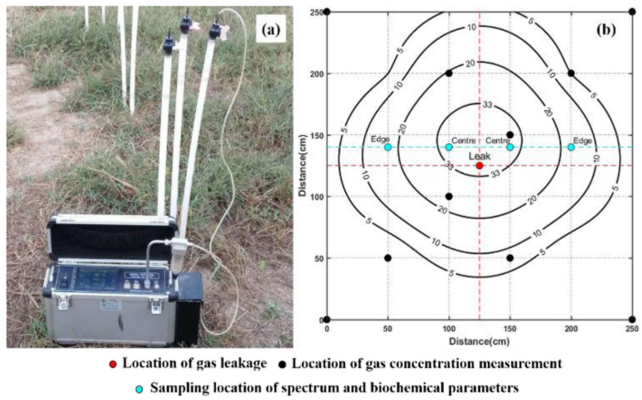

Fig. 2. (a) Methane concentration measurement. (b) Data sampling area and methane concentration distribution.

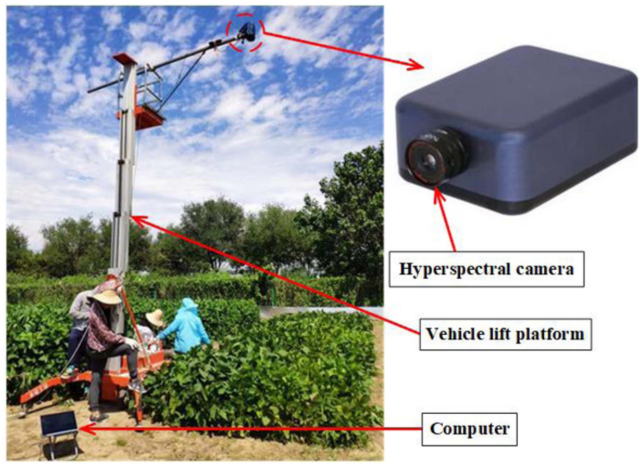

Fig. 3. Hyperspectral imagery acquisition.

plots were gas groups and the even numbered plots were control groups, as shown in Fig. 1. The adjacent plots of the gas and control groups were spaced by 0.5 m, and the interval between every two rows of plots was 1.5 m, which facilitated the passage of collection vehicles and improved the efficiency of data collection.

Natural gas is liquefied natural gas provided by gas companies, which is gasified and transported through copper pipes. Before natural gas goes underground, it is connected to the copper pipes using PVC pipes. At the edge of the plot, the PVC pipe was inserted at an angle into the soil about 0.6 m deep directly below the center of the plot. Nine small holes were drilled evenly at the bottom of the pipe to ensure that the diffusion concentration of natural gas was the same in all directions around the underground leakage point.

Wheats were seeded on September 20, 2018, with natural gas stress from October 11 to November 18. Beans were seeded on June 15, 2019, with natural gas stress dates from July 4 to September 3. Grass was seeded on June 10, 2017, with natural gas stress from July 8 to September 17. The rate of natural gas microleakage rate was controlled at 1 L/min by a computer and PLC controller during the experiment.

B. Data Collection

Fig. 2(a) shows the methane concentration measurement using the GXH-3050E infrared gas analyzer (Junfanglihua, Beijing, China). First, the instrument was turned ON and warmed up for 30 min. In addition, a rubber hose was used to connect the pipe valve to the analyzer. Then, the valve was opened and the staff recorded the peak concentration, after which the valve was closed. Soil gas concentrations at ten sampling points were measured sequentially according to the aforementioned process. Since the roots of the experimental vegetation were mainly distributed in the soil at 30 cm depth, we analyzed the methane gas concentration at a depth of 30 cm in the soil. After data interpolation and contour fitting, the concentration distribution of methane gas in soil at a depth of 30 cm was obtained [black contour in Fig. 2(b)]. The area with largest gas concentration is offset by approximately 15 cm from the leakage point [see Fig. 2(b)]. In this study, the area with a gas concentration greater than 33% were designated as the center group, the area with a gas concentration between 10% and 20% were designated as the edge group, and the area with a gas concentration of 0 were designated as the control group.

The acquisition of near ground hyperspectral imaging is shown in Fig. 3. Hyperspectral images were acquired using the SOC710e portable hyperspectral imager from Surface Optics Corporation (SOC), USA. It has an imaging spectral range of 400–1000 nm with 128 bands. Data acquisition was performed in clear and windless weather from 11:00 to 13:00. The imager was first focused, and then, fixed to the elevator platform, and the sampling process of the spectrometer was controlled by

computer. During the sampling process, the lens was aimed at the center of the plot and the height of the lens was adjusted to 5 m, while the standard plate was placed in the measurement area. The exposure time was adjusted according to the light, and each image was taken over a ground area of approximately 3.7 m × 2.8 m, which ensures that a single hyperspectral image could cover the entire plot. The spatial resolution of each image is approximately 2.8 mm × 2.8 mm. In specific experiments, five periods of image data were acquired for each vegetation type.

C. Data Preprocessing

The raw data acquired by the spectrometer is the spectral radiance brightness, which needs to be radiometrically corrected and converted to surface reflectance data, thus reducing the effects of terrain and altitude changes, image exposure, atmospheric scattering, etc., on the spectrometer imaging. The radiation correction equation is as follows:

$$R = \frac{I_O - I_D}{I_W - I_D} \tag{1}$$

where R represents the reflectance of the corrected hyperspectral image; I_O represents the radiometric brightness data of the original hyperspectral image; I_W represents the reflection data of the reference corrected whiteboard; and I_D represents the dark current data.

Due to light variations and the instrument system itself, noise may exist during hyperspectral imaging data acquisition. Therefore, it is necessary to smooth the data. In this article, a five-point weighted smoothing algorithm was used for spectral smoothing of each pixel point in the hyperspectral image. The formula is as follows:

$$R_S = \frac{1}{2.5}\left(\frac{1}{4}R_{i-2} + \frac{1}{2}R_{i-1} + R_i + \frac{1}{2}R_{i+1} + \frac{1}{4}R_{i+2}\right) \tag{2}$$

where $R_i$is the reflectance value at band i,R_S is the reflectance value after smoothing of the band, and k represents the number of bands.

The image of one period was selected as the reference image, and then, the images of other periods were registered with the same name point. After image registration, each image was cropped to a size of 900 × 900 pixels, and then, rotated 180° so that the top of the image faces north.

D. Data Analysis

The technology roadmap of the natural gas microleakage detection in this study is shown in Fig. 4. First, spectral, spatial, and temporal features of the hyperspectral images were extracted separately and fused at the feature level. Then, the target images were classified using the EC to obtain a preliminary natural gas-stressed vegetation classification map, and the classification results were optimized using mathematical morphology. Finally, the minimum external circle algorithm was used to obtain the vegetation stress range and natural gas microleakage points.

1) Feature Extraction and Fusion:

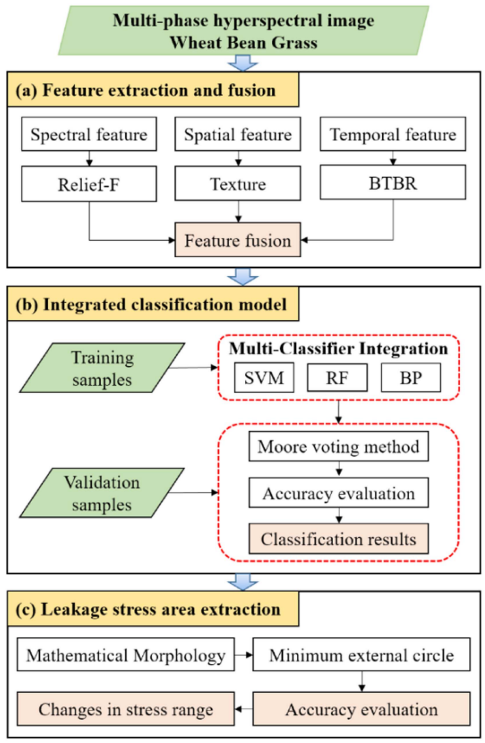

Fig. 4. Technology roadmap.

a) Spectral feature extraction: Two hundred pixels were randomly selected in the control, center, and edge group regions, respectively. The spectral mean value was taken as the spectral reflectance of the region. The weights of all bands were calculated using the Relief-F algorithm [31], ranked according to the weight magnitude, and the single band corresponding to the top 10% of optimal weights was selected and marked with a single score. The single bands corresponding to the optimal weights were calculated for all periods and all vegetation, and the single band with the highest statistical score was used as the spectral feature.

b) Texture feature extraction: The gray-level co-occurrence matrix (GLCM) is a matrix function involving pixel distances and angles, which reflects the comprehensive information of an image in terms of direction, interval, magnitude of change, and speed by calculating the correlation between the grayscale of two points at a certain distance and a certain direction in the image [32]. The GLCM can be expressed as the joint frequency distribution of the simultaneous occurrence of two grayscale pixels with a certain distance in the image. The mathematical interpretation is the probability of simultaneous appearance of pixel i as the starting point and pixel j as the ending point at a certain direction θ and distance d. In this article, four texture features were extracted using GLCM, namely variance, homogeneity, entropy, and correlation. The specific formulas are shown as follows:

$$P(i,j|d,\theta) = \{(x,y)|f(x,y) = i, f(x+dx, y+dy) = j; x, y = 0, 1, 2 \ldots, N-1\} \tag{3}$$

$$\text{Variance} = \sum_{a,b} p(a,b|d,\theta) \times (a-\mu)^2 \tag{4}$$

$$\text{Homogeneity} = \sum_{a,b} \frac{\{p(a,b|d,\theta)\}^2}{1+(a-b)^2} \tag{5}$$

$$\text{Entropy} = \sum_{a,b} p(a,b|d,\theta) \log p(a,b|d,\theta) \tag{6}$$

$$\text{Correlation} = \sum_{a,b} \frac{(a-\mu)(b-\mu)p(a,b|d,\theta)}{\text{VAR}} \tag{7}$$

where θ can be taken in four directions: 0°, 45°, 90°, and 145°. a and b represent the row number and column number of the image matrix, respectively, and $p(a,b|d,\theta)$ is the conditional probability.

c) Temporal feature extraction: The main reason for the change in the spectrum of surface vegetation is the change in the chlorophyll content and leaf area index (LAI) of the vegetation [33]. The decrease in chlorophyll content or LAI resulted in diminished absorption in the red and blue spectral domains, while the green spectral domain is less affected. The chlorophyll content or LAI of surface vegetation may change drastically under the stress of underground natural gas microleakage. In order to capture the spectral change characteristics of vegetation under natural gas microleakage, this study constructed a bitemporal band ratio model (BTBR) based on the green and red bands caused by chlorophyll change, as shown in (8). The BTBR is used to highlight the spectral characteristics of vegetation associated with natural gas microleakage stress. This index not only highlights differences in vegetation symptoms between two different stress periods but also minimizes differences in image brightness due to inconsistent calibration of the spectral imager and variations in insolation between acquisition dates [34]. This compensates to a large extent for the lack of radiometric correction of hyperspectral images, which highlights the advantage of reliable quantitative comparisons under two stress dates.

$$\text{BTBR} = \frac{(R_{Tn}/R_{T1}) - (G_{Tn}/G_{T1})}{(R_{Tn}/R_{T1}) + (G_{Tn}/G_{T1})} \tag{8}$$

where *R* and *G* represent the red and green bands of the image. *Tn* and *T1* represent phase *n* and phase 1, respectively. The calculation results of the BTBR serve as temporal characteristics for the *Tn*.

d) Feature fusion: In this article, the extracted spectral, spatial, and temporal features were fused using the feature stacking method [35]. In the fusion process, since the different types of features represent different physical meanings, the most fundamental one is the different value ranges of the type parameters, and the large value parameters may mask the recognition ability of the small value parameters. Therefore, this study needs to normalize the fused feature covariates so that the different features are in the same range of values during fusion. In this article, the extracted color and texture features are normalized to the [−1, 1] interval using min-max normalization [35].

2) Ensemble Learning Model: Ensemble learning [36] is the task of learning (classification) by generating and combining multiple basic learning algorithms, specifically by combining multiple classifiers into an integrated model by some strategy to make reliable judgments on the results. The current effective classifiers for hyperspectral image classification include SVM, RF, and back propagation (BP) neural networks. The SVM is a nonparametric supervised classifier with significant easy generalization properties by minimizing the structural risk strategy to reduce the misclassification errors of training data [37]. However, its classification performance is more significantly affected by parameters and is sensitive to regularization parameters. RF is a parameter-free machine learning method that can handle a large number of input features and it is contains multiple decision trees. It has good noise immunity and tolerance to missing data, but the running efficiency decreases significantly when the number of decision trees is large [38]. The BP neural network is a multilayer feed-forward neural network trained according to the error back propagation algorithm. It is widely used in various classification studies for its excellent nonlinear approximation performance to minimize the prediction error [39]. However, this method approximates a black-box operation and lacks a visual explanation of the classification process. All the aforementioned three methods have been widely applied in the field of hyperspectral image classification; however, each of them has certain shortcomings and limitations. The uncertainty and ambiguity of individual classifiers can be reduced by combining their results for discriminant analysis through ensemble learning. In addition, Ran et al. [40] classified stressed vegetation under natural gas microleakage based on multilevel multiscale segmentation and rotating forest classification algorithm (MMS_Ensem_RoF), which achieved good classification accuracy and detection results. Therefore, this study introduces the MMS_Ensem_RoF method to classify the fused images and analyze them in comparison with ensemble learning.

In this study, one of the gas-stressed plots and one of the control plots were selected as training images, and the others were used as validation images. The labels were divided into three categories: healthy vegetation (control group), heavily stressed vegetation (central group), and lightly stressed vegetation (edge group). Three thousand samples were selected from the hyperspectral images of each period, and each class of labels included 1000 samples. The samples were randomly divided into 60% training samples and 40% validation samples, and each class included 600 training samples and 400 validation samples.

3) Stress Range Extraction Method: The ultimate goal of this study is to detect natural gas microleakage points and to identify natural gas microleakage stress vegetation areas. Therefore, the heavily stressed and lightly stressed areas were combined as natural gas stressed vegetation areas. Based on this, mathematical morphology and the minimum external circle algorithm were applied to obtain the vegetation stress area and the location of natural gas microleakage points.

The mathematical basis of morphology is set theory, which includes four basic operations: erosion, expansion, opening, and closing [41]. These basic operations enable processing such as noise removal, edge detection and feature extraction of images [42]. After mathematical morphological processing, the natural

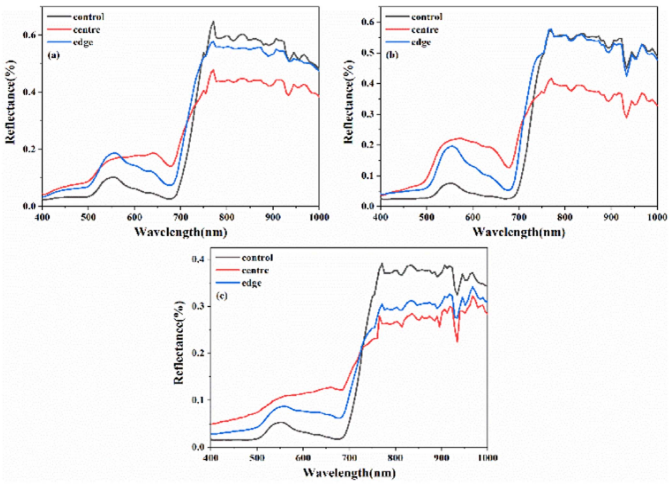

Fig. 5. Hyperspectral characteristics of vegetation under natural gas microleakage stress. (a)—(c) Wheat, bean, and grass, respectively.

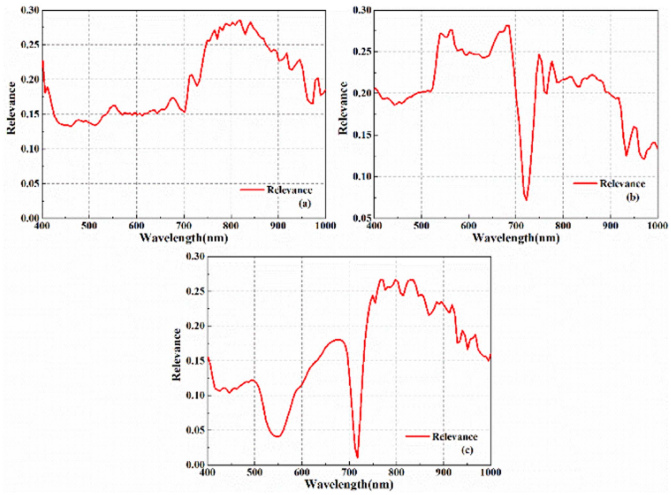

Fig. 6. Single band weight values based on the Relief-F algorithm. (a)–(c) Wheat, bean, and grass, respectively.

gas microleakage stress region appears as an irregular circle-like shape in the image. The connected objects in the central region of the image were extracted using the minimum external circle algorithm. The extracted fitted circle was used to represent the vegetation stress range of natural gas microleakage, and the center of this fitted circle was used as the location of the natural gas microleakage point.

III. Results

A. Feature Extraction and Fusion Results

1) Spectral Feature: The hyperspectral reflectance of wheat, bean, and grass is shown in Fig. 5. In the visible region of 400–730 nm, the spectral reflectance of the vegetation in both the center and edge groups was greater than that of the control group. In addition, the spectral reflectance of the center group was greater than that of the edge group, indicating that the vegetation in the center group was more affected by natural gas microleakage stress. In the NIR region of 760–1000 nm, the spectral reflectance of vegetation in both the control and edge groups was greater than that of vegetation in the center group. The aforementioned spectral changes may be due to the fact that the increased concentration of subsurface natural gas changes the original air components in the soil, leading to a decrease in oxygen content [43], making the vegetation roots less capable of aerobic respiration and nutrient uptake. The decrease in root absorption capacity seriously affects the normal growth of vegetation [44], resulting in a decrease in chlorophyll content or biomass of vegetation, which leads to changes in the spectral response of vegetation [45].

The band weights of each hyperspectral image for wheat, bean, and grass were calculated separately using the Relief-F algorithm, as shown in Fig. 6. The larger the weight of the bands, the greater the ability to discriminate between vegetation stressed by different concentrations of natural gas microleakage. The most relevant single band of wheat and grass was in the range of 750–850 nm, and the most relevant single band of bean was in the range of 550–690 nm. The Relief-F feature processing was carried out on the spectral information of all the stressed periods of the three vegetation species. For the single-band weight results of each phase, the band with the top 10% weight was selected as the optimal candidate band and marked as one score. Finally, the single band with the highest score was selected as the spectral feature of the hyperspectral image. The selected characteristic bands are shown in Table I.

TABLE I
Multiclass Hyperspectral Image Fusion Features

Feature type	Number	Feature parameter
Spectral feature	10	565,659,674,685,760, 776,787,792,803,841nm
Spatial feature	40	Variance, Homogeneity, Entropy, Correlation
Temporal feature	1	BTBR

2) Texture Features: Texture features such as variance, homogeneity, entropy, and correlation were extracted from the feature band images (as shown in Fig. 7). The values of variance, entropy, and correlation of vegetation in the natural gas leakage stress area were larger than those of healthy vegetation, which were shown in high brightness in the image. The homogeneity value of the coerced vegetation was less than that of the healthy vegetation, which was shown in low brightness in the image. In addition, the texture distribution of vegetation in natural gas-stressed areas was complex, and there was some variability in texture in areas with different degrees of natural gas stress. In this study, texture features were extracted from grayscale images in the feature bands, and finally, 40 texture features were obtained from hyperspectral images.

3) Temporal Features: Based on the single-band feature screening results, 690 and 530 nm were selected as the red and green bands for calculating the BTBR. The temporal features of the three vegetation hyperspectral images are shown in Fig. 8.

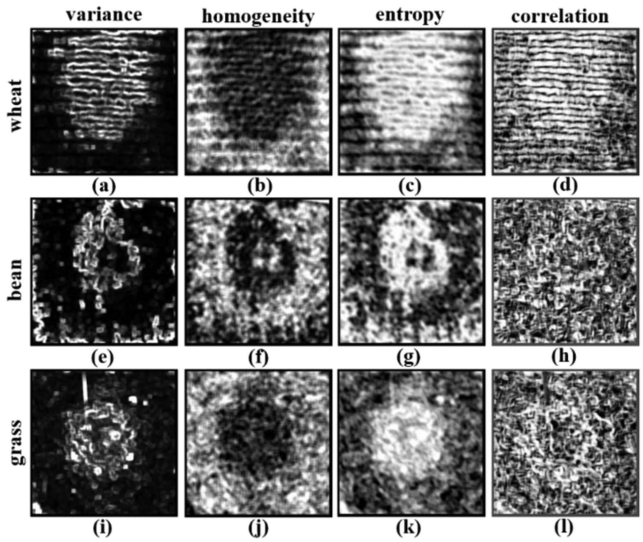

Fig. 7. Vegetation texture images under natural gas microleakage stress. (a)–(d) Texture feature image of wheat. (e)–(h) Texture feature image of bean. (i)–(l) Texture feature image of grass.

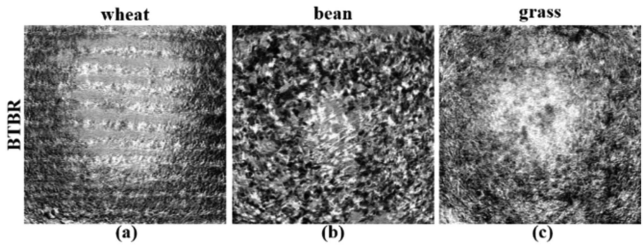

Fig. 8. Temporal characteristics of natural gas microleakage stress on vegetation. (a)–(c) Wheat, bean, and grass, respectively.

The BTBR of vegetation in the natural gas microleakage stressed area was larger than that of healthy vegetation, which is highlighted in the image. As can be seen from Fig. 8, the range of temporal features changes in wheat and grass under natural gas stress is greater than that of bean, which better captures the changing characteristics of the stressed vegetation at different times. This is because bean plants are higher than wheat and grass, and the branches and leaves of bean in the edge group will extend to the center group due to continuous growth.

4) Feature Fusion: Ten spectral features, forty spatial texture features, and one temporal phase feature were obtained in this study (as shown in Table I). Then, the spectral, spatial, and temporal features were fused at the feature level to improve the robustness of subsequent classification models and the interpretability of natural gas microleakage stress features. Therefore, the fused data include a total of 51 features.

B. Feature-Fusion-Based Classification Results

An ensemble classification model was established based on the fused multifeature image data. The ensemble classification model includes three individual classifiers, namely SVM, RF, and BP. The labels of the vegetation in the control, center, and edge groups are assigned as 0, 1, and 2 during the sample training. The optimal model parameters of the individual classifier were determined based on multiple training sessions. The optimal parameters of the SVM model are $C = 80$ and gamma $= 0.12$. The optimal parameters of the RF model are n_estimators $= 100$, min_samples_split $= 7$, and min_samples_leaf $= 2$. The optimal parameters of the BP neural network model are $\lambda = 0.001$, and batch_size $= 100$. A fivefold cross-validation was used to improve the accuracy and confidence of the model. Finally, the classification results of individual classifiers were passed through the Moore voting method to obtain the final classification results. In addition, this study referred to the MMS_Ensen_RoF model parameter settings of Ran et al. [40]. The number of base classifiers and the number of feature subsets in the RoF classification algorithm were set to 10 and 35, respectively. The final image classification results were achieved by the mean of ten Monte Carlo runs.

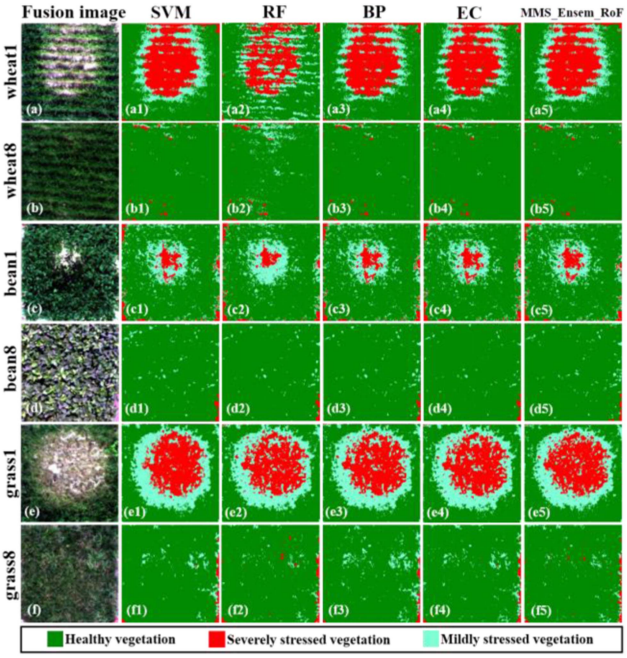

Fig. 9. Vegetation classification results under natural gas microleakage stress based on multifeature fusion. (a)–(b5) Classification results of wheat-stressed and control plots, respectively. (c)–(d5) Classification results of bean-stressed and control plots, respectively. (e)–(f5) Classification results of grass-stressed and control plots, respectively.

The classification results of the validated images of wheat, bean, and grass are shown in Fig. 9. The average overall classification accuracies (OA) of the training and validation sets are shown in Table II. The overall classification accuracy of wheat, bean, and grass were 94.52%, 93.94%, and 96.40%, respectively. Compared with individual classifiers, the EC model obtains optimal classification accuracy on both training and validation images. For the bean and grass, the classification accuracy based on MMS_Ensen_RoF was higher than that of Ran et al. [40]. This is because this study fully employs spectral-spatial-temporal features for image classification, and Ran et al. [40] only used spectral and spatial features. It demonstrates that the inclusion of

TABLE II
OVERALL ACCURACY OF VEGETATION CLASSIFICATION UNDER NATURAL GAS MICROLEAKAGE STRESS BASED ON MULTIFEATURE FUSION

	Type	Classification model				
		SVM	RF	BP	EC	MMS_Ensen_RoF
Training result(%)	Wheat	96.34	91.83	95.66	97.32	95.24
	Bean	95.45	90.86	95.13	96.85	94.57
	Grass	98.28	97.63	96.52	98.89	96.76
Verification result(%)	Wheat	93.67	87.99	93.92	94.52	93.78
	Bean	93.33	87.33	93.49	93.94	92.56
	Grass	95.68	95.20	95.89	96.40	95.73

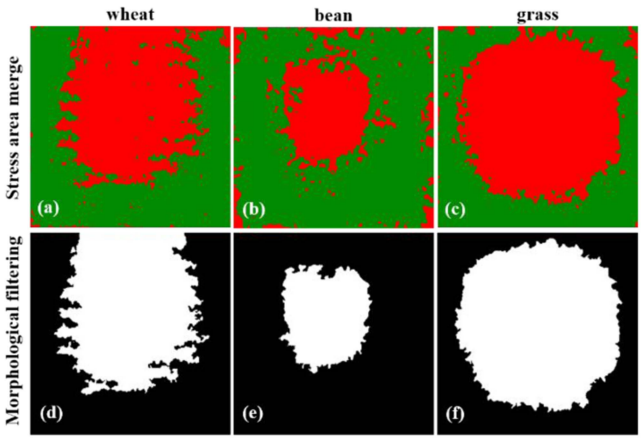

Fig. 10. Extracting vegetation stress regions from natural gas microleakage based on multifeature fusion. (a)–(c) Result of class merging of wheat, bean, and grass, respectively. (d)–(f) Results of mathematical morphology treatment of wheat, bean, and grass, respectively.

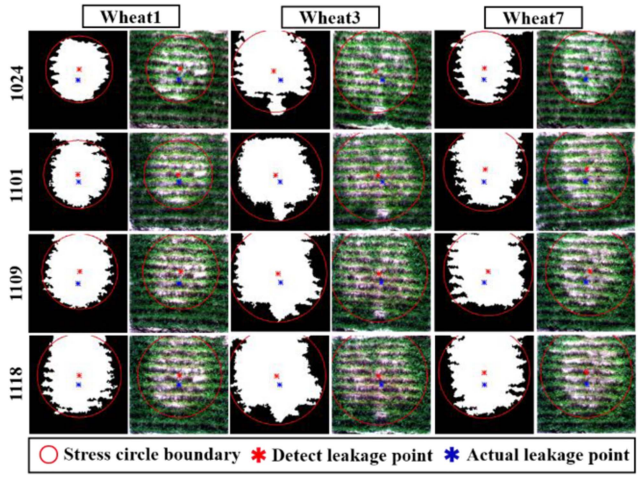

Fig. 11. Identification results of wheat under natural gas microleakage stress at different periods.

temporal features can better characterize the differences between stressed and healthy vegetation and obtain better classification results. The overall classification accuracy of bean was lower than that of wheat and grass, which may be due to the phenomenon of superimposed shading caused by the expansion of bean branches in all directions [see Fig. 9(c)]. The edge areas of the control plots were easily misidentified as heavily stressed vegetation due to the bare soil at the edges of the plots; in addition, some shaded areas in the control plots were easily misidentified as lightly stressed vegetation. The misidentified regions of the control plots are all scattered and optimized by mathematical morphological operations.

C. Natural Gas Microleakage Stresses Vegetation Extraction

In this study, heavily stressed vegetation and lightly stressed vegetation were merged as in Fig. 10(a)–(c). After merging, the red areas were stressed vegetation and the green areas were healthy vegetation. It can be seen that the range of vegetation stress was irregularly circular, containing many small spots or voids. The image was poorly connected and closed, especially in the edge areas of the bean plots. The reason for the aforementioned results may be that leaves overlap and cross each other during natural gas microleakage stress and vegetation growth and development. Shadows and bare soil tend to appear during image acquisition, affecting the boundaries and integrity of the classification results [46]. In order to improve the aforementioned situation, this study uses a mathematical morphology algorithm to perform erosion, expansion, and opening and closing operations on the merged images, which can effectively remove the internal speckles and voids in the target and smooth the target boundary. The processing results are shown in Fig. 10(d)–(f).

The range of vegetation stress and the location of leakage points of the image were extracted using the minimum external circle, as shown in Figs. 11–13. Fig. 11 shows the identification results of wheat under natural gas microleakage stress at different periods. On October 24, the center group of wheat was subjected to natural gas stress, resulting in light green symptoms on the leaves and short and sparse plants. It can be seen from Fig. 11 that the areas of natural gas microleakage stress were not the same in different plots, which may be related to the diffusion range of methane gas, the growth state of the vegetation, or the external environment [47]. On November 1, the extent of stress increased further in all plots. Wheat stress symptoms were more severe in the center group, with the leaf color gradually changing from the initial light green to light yellow. The light green characteristics of wheat in the edge group were more obvious. From November 9 to November 18, the stress range of wheat

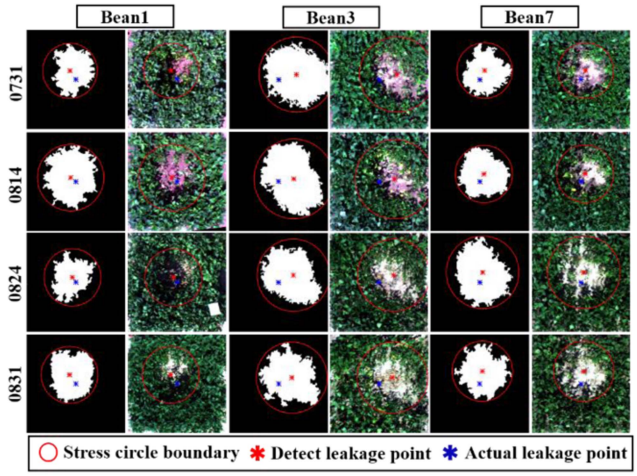

Fig. 12. Identification results of bean under natural gas microleakage stress at different periods.

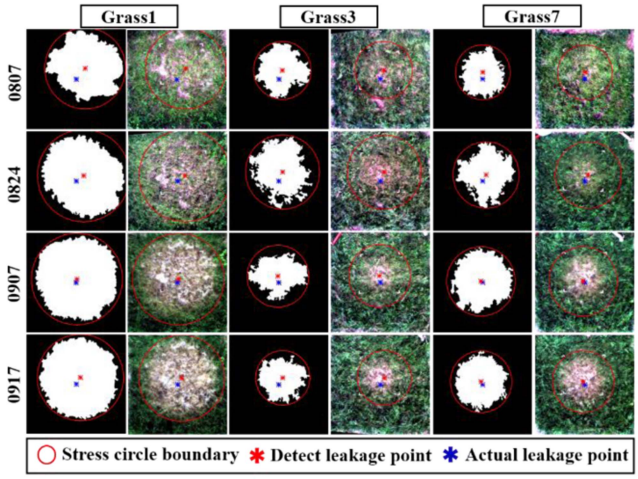

Fig. 13. Identification results of grass under natural gas microleakage stress at different periods.

has been expanding continuously, and the stress symptoms have become more severe.

Fig. 12 shows the identification results of bean under natural gas microleakage stress at different periods. On July 30, beans showed obvious symptoms of stress, with sparse growth and dwarf vegetation in the center group, and most leaves had turned yellow or brown. The central area of the plot had relatively clear bare soil. The leaves of bean in the edge group were light green. The distance between the detected leakage point and the actual leakage point in plot Bean3 is far, which may be due to the slow growth of bean at the edge, resulting in the appearance of obvious bare soil, making the detection error larger. On August 14, the bean stress range showed an increasing trend. The bean in the center group grew slowly, with sparse branching and more severe yellowing. From August 24 to August 31, the stress range of bean gradually decreased.

Fig. 13 shows the identification results of grass under natural gas microleakage stress at different periods. On August 7, the

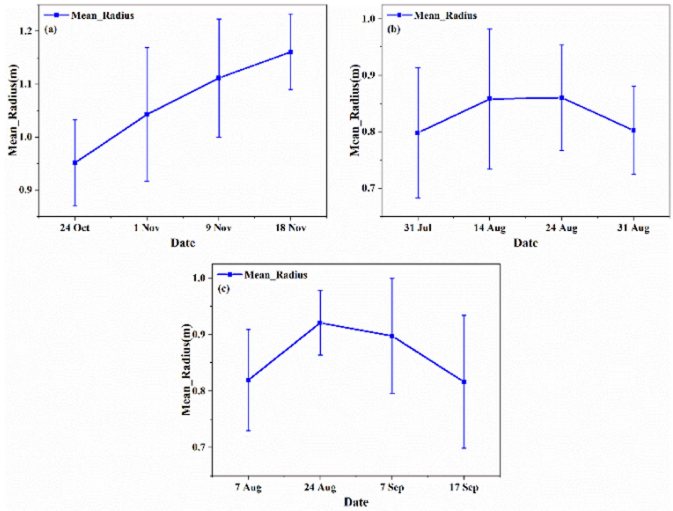

Fig. 14. Variation pattern of vegetation stress range of natural gas microleakage. (a)–(c) Wheat, bean, and grass, respectively. (Vertical bars indicate standard deviation.)

stress symptoms of grass were less severe. In the center group, there was slight yellowing of the leaves and uneven distribution of bare soil. In addition, the stress range of Grass1 was larger. This is because the growth condition of Grass1 before aeration was poorer, so the stress symptoms were more severe after aeration. On August 24, the stress range of the grass increased further. This was due to the unstable growth of grass in the center group, which was prone to growth stagnation or even death, resulting in an increase in the stress range in the center group. On September 7, there were some differences in stress range changes in the grass plots, with a significant decrease in the Grass3 plot and a slight increase in the other plots. On September 17, the grass showed a trend of decreasing stress extent.

D. Spatial and Temporal Changes in Stressed Vegetation

Table III shows MALE of natural gas microleakage points and the extent of stressed vegetation for the three vegetation species at different periods. The MALE represents the mean value of the distance between the detected natural gas microleakage point and the actual natural gas microleakage point [17]. Except for Bean3, the MALE of natural gas microleakage points were less than 0.4 m. The MALE of natural gas microleakage points in wheat, bean, and grass were 0.27, 0.30, and 0.23 m, respectively. The MALE of natural gas microleakage point of bean was the largest, followed by wheat and grass. The natural gas microleakage stress radius ranged from 0.7 to 1.25 m for the three vegetation types. The wheat plots had the largest average stress radius of 1.07 m, while the bean and grass had average stress radius of 0.83 and 0.86 m, respectively.

Fig. 14 shows the changes in the stress range of three vegetation species under natural gas microleakage over time. The mean stress radius of wheat plots increased with increasing stress time. From October 24 to November 1, wheat was more sensitive to natural gas stress, so its stress range increased rapidly. From November 1 to November 18, wheat was less sensitive to natural

TABLE III
STRESS RANGE AND LOCALIZATION POINT IDENTIFICATION ACCURACY OF NATURAL GAS MICROLEAKAGE BASED ON MULTIFEATURE FUSION

Vegetation	Date\Plot	MALE(m)			Mean_ MALE(m)		Radius(m)			Mean_ Radius(m)	
		P1	P3	P7			P1	P3	P7		
Wheat	1024	0.28	0.29	0.29	0.29	0.27	0.86	1.06	0.94	0.95	1.07
	1101	0.19	0.20	0.32	0.24		0.88	1.18	1.07	1.04	
	1109	0.31	0.23	0.30	0.28		0.97	1.24	1.13	1.11	
	1118	0.24	0.23	0.31	0.26		1.07	1.25	1.16	1.16	
Bean	0731	0.27	0.47	0.22	0.32	0.30	0.70	0.96	0.71	0.80	0.83
	0814	0.17	0.40	0.26	0.28		0.85	1.01	0.73	0.86	
	0824	0.15	0.42	0.33	0.28		0.73	0.92	0.93	0.86	
	0831	0.28	0.37	0.27	0.33		0.73	0.91	0.77	0.80	
Grass	0807	0.39	0.37	0.17	0.31	0.23	0.91	0.85	0.70	0.82	0.86
	0824	0.33	0.25	0.18	0.25		0.98	0.94	0.84	0.92	
	0907	0.25	0.16	0.05	0.15		1.03	0.79	0.87	0.90	
	0917	0.30	0.20	0.09	0.19		0.97	0.69	0.78	0.82	

gas stress and the stress range increased at a decreasing rate. The stress radius of both bean and grass showed a trend of increasing, and then, decreasing with the increasing leakage time, but there were differences in the intensity of the changes. The range of stress in bean changed relatively slowly. There was no significant change in the radius of stress in bean from August 14 to August 24. The range of stress in the grass changed more significantly. From August 7 to August 24, the radius of stress in the grass increased faster, while from August 24 to September 17, the radius of stress in the grass decreased faster. This may be because grass has a shallower root system than bean and its growth condition was easily affected by external environmental stress.

IV. DISCUSSION

As the concentration of natural gas in the soil increases, the O_2 concentration around the root system of vegetation decreases [see Fig. 2(b)], which causes a low-oxygen environment directly. This will seriously affect the respiration and absorption capacity of the root system, indirectly hindering the normal growth of leaves and leading to a decrease in chlorophyll content, which has been verified in [45] and [48]. The spectral features of vegetation extracted in this study (see Table I) were uniformly distributed in the visible (green and red light bands) as well as in the short-wave near-infrared region. These spectral features were closely related to both chlorophyll content and water content [49], [50], [51], effectively explaining the differences in spectral changes of vegetation under natural gas microleakage stress. In addition, natural gas stress was more severe in the center group of the plot, resulting in shorter vegetation and more bare soil. It makes the texture features of the center group area more different from the edge group and control group (see Fig. 7). This plays a positive role in extracting the natural gas microleakage stress areas. It is worth noting that this study collected hyperspectral imagery under multiple stress periods, which has a great advantage over single-date data sources. This is because stress symptoms similar to natural gas microleakage can easily occur in single date scenarios with differences in phenology, differences in vegetation growth conditions, or other stressful pressures. The spectral features or texture features at a single time can easily confuse different types of stress symptoms, while temporal features based on multitemporal hyperspectral imagery provide temporal features that help to eliminate anomalies other than natural gas microleakage stress, and provide an additional reliable basis for accurate identification of natural gas microleakage points.

As natural gas microleakage continued, the extent of stress and the degree of stress in the wheat plots increased, which may include the following two reasons. First, underground natural gas microleakage continuously squeezes oxygen from the soil, which affects the uptake of nutrients and water by the roots [52], resulting in the gradual chlorosis of wheat leaves and their increasing extent. Second, wheat enters the overwintering period in mid-November. The growth and development of wheat started to become slow and the metabolic rate decreased. This makes previously healthy wheat susceptible to natural gas stress as it enters the overwintering period, which further increases the range of stressed wheat. In the later stage of natural gas microleakage, the stress range of bean and grass showed a decreasing trend. This may be due to the fact that the roots of vegetation in the edge group would grow toward the area of lower natural gas concentration and their root systems gradually stabilized, thus gradually adapting to the low natural gas concentration environment and allowing the bean and grass in the edge group to return to normal growth [11]. However, the vegetation in the center group showed increasingly significant stress symptoms. This is because it is difficult for most of the vegetation to grow

back under the high concentration of natural gas, resulting in more and more bare soil in the center group.

There are differences in the localization of natural gas microleakage point detection in different vegetation, which may be related to the canopy morphology of the vegetation. The plant height of beans is relatively high, and the growth of branches and leaves is relatively disorderly, which makes the leaves in the stress area cross-distribute each other, and the canopy structure is not uniform, resulting in an irregular shape of the stress area [47]. Therefore, the localization error of bean is large. The distribution of grass on the canopy is more dense and uniform than that of wheat and the stress area is closer to the circle-like shape, so the localization error is smaller. This is consistent with the natural gas microleakage point localization errors in Table III.

The radius of natural gas microleakage stress for the three vegetation types ranged from 0.7 to 1.25 m as shown in Table III. This is relatively similar to the spatial pattern of gas leak stress vegetation found in other experimental studies. Smith et al. [11] found that natural gas leakage resulted in a circular stress zone of 0.5–1 m near the leakage point. Male et al. [15] found that the range of stressed vegetation was roughly 1 m after 5 days of CO_2 leakage; the range of stressed vegetation increased to 2.5 m after 10 days of leakage. Similarly, Al-Traboulsi et al. [53] observed the vegetation around the leakage point formed a circular stress area with a diameter of 1–1.2 m through CO_2 leakage experiments. The mean stress radius of wheat, bean, and grass in all periods was 1.07, 0.83, and 0.86 m, respectively, indicating differences in the range of natural gas stress in different types of vegetation. Hoeks [54] found that the radius of the vegetation stress area due to subsurface gas leakage might range from 1 to 15 m, which is related to the rate of subsurface gas leakage, soil physicochemical properties, and vegetation type. In this study, soil conditions (water content, porosity, etc.) may differ among plots; second, the stress response of different vegetation to natural gas stress is also different. These may be the reasons why the range of stress is not the same for different vegetation.

In this study, spectral, spatial, and temporal features were extracted from hyperspectral images and fused at the feature level. The fused data not only assemble spectral-spatial-temporal features but also reduces the high-dimensional features (128 bands) of the original hyperspectral image to 51 features, which reduces the computational complexity of the subsequent classification model to some extent. As can be seen from Table II, the classification accuracies of ensemble learning are all higher than other individual classifiers. On the one hand, it reflects the effective integration of individual classifiers by the Moore voting method in ensemble learning [55], and on the other hand, it provides solid conditions for the accurate identification and extraction of natural gas microleakage-stressed vegetation. Although there were some differences in the degree of response of different vegetation to natural gas microleakage stress, the natural gas leakage localization errors of all experimental plots were lower than 0.4 m, and the localization results were relatively accurate. From the practical application point of view, the ensemble learning method based on spectral, spatial, and temporal features proposed in this study can provide technical support for large-scale detection of natural gas microleakage in underground storage reservoirs or pipelines in the field. From the practical application point of view, the method proposed in this study can provide technical support for large-scale detection of natural gas microleakage in underground gas storage reservoirs or pipelines in the field. It should be mentioned that with the continuous improvement of remote sensing technology, there is a great potential for efficient detection of natural gas microleakage using satellite remote sensing.

V. Conclusion

Microleakage in underground natural gas storage can be a serious hazard to the economy, environment, and public safety, so it is necessary to detect and determine the natural gas microleakage points in a timely manner. However, three issues in detecting natural gas microleakage need to be further explored, including the extraction and utilization of temporal features in hyperspectral images, the accurate classification of ensemble classification in images, and the analysis of spatial and temporal changes in vegetation stress areas under natural gas microleakage. The solution of the aforementioned problems is crucial for the accurate detection of natural gas microleakage. Therefore, this study proposes a natural gas microleakage stress vegetation detection model that integrates spectral, spatial, and temporal features using multitemporal hyperspectral imagery and ensemble classification strategy.

The main findings of this article are as follows.

1) Ten feature bands (565, 659, 674, 685, 760, 776, 787, 792, 803, and 841 nm) were screened from 128 bands of hyperspectral images using the Relief-F algorithm. Based on this, four spatial texture features (variance, homogeneity, entropy, and correlation) of each feature band image were extracted using GLGM. The temporal features of the images were extracted using the BTBR temporal index.
2) Feature-level fusion of the aforementioned extracted spectral, spatial, and temporal phase feature components was performed. The fused images of wheat, bean, and grass were classified using the ensemble classification with an average overall accuracy of 94.52%, 93.94%, and 96.40%, respectively, outperforming the individual classifiers.
3) Finally, the range of natural gas microleakage stress vegetation and the localization of the leakage point were extracted by mathematical morphology and minimum external circle algorithm. The MALE of natural gas microleakage point identification results for all three vegetation types is less than 0.3 m, among which the MALE of wheat and grass are 0.27 and 0.23 m, respectively.

The results indicate that the overall accuracy of natural gas microleakage identification is high and meets the practical application requirements. In addition, the mean values of stress radius for wheat, bean, and grass were 1.07, 0.83, and 0.86 m, respectively. With the microleakage of natural gas, the stress radius of wheat gradually increased, and the stress radius of bean and grass first increased, and then, decreased, indicating that different types of vegetation exhibited their own unique spatial characteristics of stress. Researchers can determine the natural gas microleakage information based on the spatial

variation characteristics of different stressed vegetation on the surface. The proposed method provides a reference for identifying vegetation stress in multitemporal hyperspectral images and provides a theoretical basis for future natural gas microleakage detection in large-scale underground gas storage or pipeline on a satellite-based platform.

REFERENCES

[1] C. Liu, T. Lao, W.-Z. Wu, W. Xie, and H. Zhu, "An optimized nonlinear grey Bernoulli prediction model and its application in natural gas production," *Expert Syst. Appl.*, vol. 194, 2022, Art. no. 116448, doi: 10.1016/j.eswa.2021.116448.

[2] J. Li, W. Liang, Y. Chen, Y. Qiu, H. Li, and S. Zhang, "Study on gas leakage along cement sheath interfaces in salt cavern gas storage well," *J. Natural Gas Sci. Eng.*, vol. 103, 2022, Art. no. 104621, doi: 10.1016/j.jngse.2022.104621.

[3] A. Schimmelmann et al., "Natural geological seepage of hydrocarbon gas in the Appalachian Basin and Midwest USA in relation to shale tectonic fracturing and past industrial hydrocarbon production," *Sci. Total Environ.*, vol. 644, pp. 982–993, 2018, doi: 10.1016/j.scitotenv.2018.06.374.

[4] J. Woda et al., "Methane concentrations in streams reveal gas leak discharges in regions of oil, gas, and coal development," *Sci. Total Environ.*, vol. 737, 2020, Art. no. 140105, doi: 10.1016/j.scitotenv.2020.140105.

[5] X. Pan, J. Jiang, and Y. Xiao, "Identifying plants under natural gas microleakage stress using hyperspectral remote sensing," *Ecol. Inform.*, vol. 68, 2022, Art. no. 101542, doi: 10.1016/j.ecoinf.2021.101542.

[6] P. Bérest, A. Réveillère, D. Evans, and M. Stöwer, "Review and analysis of historical leakages from storage salt caverns wells," *Oil Gas Sci. Technol.*, vol. 74, 2019, doi: 10.2516/ogst/2018093.

[7] I. D. Sanches, C. R. Souza Filho, L. A. Magalhães, G. C. M. Quitério, M. N. Alves, and W. J. Oliveira, "Assessing the impact of hydrocarbon leakages on vegetation using reflectance spectroscopy," *ISPRS J. Photogramm. Remote Sens.*, vol. 78, pp. 85–101, 2013.

[8] D. Schumacher, "Surface geochemical exploration for oil and gas: New life for an old technology," *Lead. Edge*, vol. 19, no. 3, pp. 258–261, 2000, doi: 10.1190/1.1438582.

[9] P. Arellano, K. Tansey, H. Balzter, and D. S. Boyd, "Detecting the effects of hydrocarbon pollution in the Amazon forest using hyperspectral satellite images," *Environ. Pollut.*, vol. 205, pp. 225–239, 2015, doi: 10.1016/j.envpol.2015.05.041.

[10] G. Lassalle et al., "Application of PROSPECT for estimating total petroleum hydrocarbons in contaminated soils from leaf optical properties," *J. Hazard. Mater.*, vol. 377, pp. 409–417, 2019, doi: 10.1016/j.jhazmat.2019.05.093.

[11] K. L. Smith, M. D. Steven, and J. J. Colls, "Use of hyperspectral derivative ratios in the red-edge region to identify plant stress responses to gas leaks," *Remote Sens. Environ.*, vol. 92, no. 2, pp. 207–217, 2004, doi: 10.1016/j.rse.2004.06.002.

[12] G. Lassalle, A. Credoz, R. Hédacq, S. Fabre, D. Dubucq, and A. Elger, "Assessing soil contamination due to oil and gas production using vegetation hyperspectral reflectance," *Environ. Sci. Technol.*, vol. 52, no. 4, pp. 1756–1764, 2018, doi: 10.1021/acs.est.7b04618.

[13] H. M. A. van der Werff, W. H. Bakker, F. D. van der Meer, and W. Siderius, "Combining spectral signals and spatial patterns using multiple Hough transforms: An application for detection of natural gas seepages," *Comput. Geosci.*, vol. 32, no. 9, pp. 1334–1343, 2006, doi: 10.1016/j.cageo.2005.12.003.

[14] M. F. Noomen, H. M. A. van der Werff, and F. D. van der Meer, "Spectral and spatial indicators of botanical changes caused by long-term hydrocarbon seepage," *Ecol. Inform.*, vol. 8, pp. 55–64, 2012, doi: 10.1016/j.ecoinf.2012.01.001.

[15] E. J. Male et al., "Using hyperspectral plant signatures for CO_2 leak detection during the 2008 ZERT CO_2 sequestration field experiment in Bozeman, Montana," *Environ. Earth Sci.*, vol. 60, no. 2, pp. 251–261, 2010, doi: 10.1007/s12665-009-0372-2.

[16] M. Noomen, A. Hakkarainen, M. van der Meijde, and H. van der Werff, "Evaluating the feasibility of multitemporal hyperspectral remote sensing for monitoring bioremediation," *Int. J. Appl. Earth Obs. Geoinf.*, vol. 34, no. 1, pp. 217–225, 2015, doi: 10.1016/j.jag.2014.08.016.

[17] J. Jiang, W. Ran, K. Xiong, and Y. Pan, "A spectral-spatial approach for detection of single-point natural gas leakage using hyperspectral imaging," *Int. J. Greenhouse Gas Control*, vol. 103, no. 11, 2020, Art. no. 103181, doi: 10.1016/j.ijggc.2020.103181.

[18] Y. Du, J. Jiang, Z. Liu, and Y. Pan, "Combining a crop growth model with CNN for underground natural gas leakage detection using hyperspectral imagery," *IEEE J. Sel. Topics Appl. Earth Observ. Remote Sens.*, vol. 15, pp. 1846–1856, 2022, doi: 10.1109/JSTARS.2022.3150089.

[19] C. Gómez, J. C. White, and M. A. Wulder, "Optical remotely sensed time series data for land cover classification: A review," *ISPRS J. Photogramm. Remote Sens.*, vol. 116, pp. 55–72, 2016, doi: 10.1016/j.isprsjprs.2016.03.008.

[20] D. P. Roy, Y. Jin, P. E. Lewis, and C. O. Justice, "Prototyping a global algorithm for systematic fire-affected area mapping using MODIS time series data," *Remote Sens. Environ.*, vol. 97, no. 2, pp. 137–162, 2005, doi: 10.1016/j.rse.2005.04.007.

[21] Y. Shi et al., "Partial least square discriminant analysis based on normalized two-stage vegetation indices for mapping damage from rice diseases using PlanetScope datasets," *Sensors*, vol. 18, no. 6, pp. 1901, 2018, doi: 10.3390/s18061901.

[22] J. Verbesselt, R. Hyndman, G. Newnham, and D. Culvenor, "Detecting trend and seasonal changes in satellite image time series," *Remote Sens. Environ.*, vol. 114, no. 1, pp. 106–115, 2010, doi: 10.1016/j.rse.2009.08.014.

[23] J. Anderegg, K. Yu, H. Aasen, A. Walter, F. Liebisch, and A. Hund, "Spectral vegetation indices to track senescence dynamics in diverse wheat germplasm," *Front. Plant Sci.*, vol. 10, pp. 1–20, 2020, doi: 10.3389/fpls.2019.01749.

[24] W. A. Dorigo, R. Zurita-Milla, A. J. W. de Wit, J. Brazile, R. Singh, and M. E. Schaepman, "A review on reflective remote sensing and data assimilation techniques for enhanced agroecosystem modeling," *Int. J. Appl. Earth Observ. Geoinf.*, vol. 9, no. 2, pp. 165–193, 2007, doi: 10.1016/j.jag.2006.05.003.

[25] T. Rumpf, A. K. Mahlein, U. Steiner, E. C. Oerke, H. W. Dehne, and L. Plümer, "Early detection and classification of plant diseases with support vector machines based on hyperspectral reflectance," *Comput. Electron. Agriculture*, vol. 74, no. 1, pp. 91–99, 2010, doi: 10.1016/j.compag.2010.06.009.

[26] L. Tian et al., "Spectroscopic detection of rice leaf blast infection from asymptomatic to mild stages with integrated machine learning and feature selection," *Remote Sens. Environ.*, vol. 257, 2021, Art. no. 112350, doi: 10.1016/j.rse.2021.112350.

[27] H. Shen, Y. Lin, Q. Tian, K. Xu, and J. Jiao, "A comparison of multiple classifier combinations using different voting-weights for remote sensing image classification," *Int. J. Remote Sens.*, vol. 39, no. 11, pp. 3705–3722, 2018, doi: 10.1080/01431161.2018.1446566.

[28] M. R. Smith and T. Martinez, "The robustness of majority voting compared to filtering misclassified instances in supervised classification tasks," *Artif. Intell. Rev.*, vol. 49, no. 1, pp. 105–130, 2018, doi: 10.1007/s10462-016-9518-2.

[29] D. Yuan, J. Jiang, X. Qi, Z. Xie, and G. Zhang, "Selecting key wavelengths of hyperspectral imagine for nondestructive classification of moldy peanuts using ensemble classifier," *Infrared Phys. Technol.*, vol. 111, no. 11, 2020, Art. no. 103518, doi: 10.1016/j.infrared.2020.103518.

[30] H. Yao et al., "Combination of hyperspectral and quad-polarization SAR images to classify marsh vegetation using stacking ensemble learning algorithm," *Remote Sens.*, vol. 14, no. 21, 2022, Art. no. 5478, doi: 10.3390/rs14215478.

[31] M. Robnik-Šikonja and I. Kononenko, "Theoretical and empirical analysis of ReliefF and RReliefF," *Mach. Learn.*, vol. 53, pp. 23–69, 2003, [Online]. Available: http://lkm.fri.uni-lj.si/xaigor/slo/clanki/MLJ2003-FinalPaper.pdf

[32] G. E. Meyer, T. Mehta, M. F. Kocher, D. A. Mortensen, and A. Samal, "Textural imaging and discriminant analysis for distinguishing weeds for spot spraying," *Trans. Amer. Soc. Agriculture Eng.*, vol. 41, no. 4, pp. 1189–1197, 1998, doi: 10.13031/2013.17244.

[33] A. R. Huete, H. Q. Liu, K. Batchily, and W. Van Leeuwen, "A comparison of vegetation indices over a global set of TM images for EOS-MODIS," *Remote Sens. Environ.*, vol. 59, no. 3, pp. 440–451, 1997.

[34] W. Dorigo and A. Lucieer, "Mapping invasive Fallopia japonica by combined spectral, spatial, and temporal analysis of digital orthophotos," *Int. J. Appl. Earth Observ. Geoinf.*, vol. 19, pp. 185–195, 2012, doi: 10.1016/j.jag.2012.05.004.

[35] M. Fauvel, J. A. Benediktsson, J. Chanussot, and J. R. Sveinsson, "Spectral and spatial classification of hyperspectral data using SVMs and morphological profiles," *IEEE Trans. Geosci. Remote Sens.*, vol. 46, no. 11, pp. 3804–3814, Nov. 2008, doi: 10.1109/TGRS.2008.922034.
[36] X. Dong, Z. Yu, W. Cao, Y. Shi, and Q. Ma, "A survey on ensemble learning," *Front. Comput. Sci.*, vol. 14, no. 2, pp. 241–258, 2020, doi: 10.1007/s11704-019-8208-z.
[37] J. Hu, J. Wang, and G. Zeng, "A hybrid forecasting approach applied to wind speed time series," *Renew. Energy*, vol. 60, pp. 185–194, 2013.
[38] M. Belgiu and L. Drăgu, "Random forest in remote sensing: A review of applications and future directions," *ISPRS J. Photogramm. Remote Sens.*, vol. 114, pp. 24–31, 2016, doi: 10.1016/j.isprsjprs.2016.01.011.
[39] A. I. De Castro, R. Ehsani, R. Ploetz, J. H. Crane, and J. Abdulridha, "Optimum spectral and geometric parameters for early detection of laurel wilt disease in avocado," *Remote Sens. Environ.*, vol. 171, pp. 33–44, 2015, doi: 10.1016/j.rse.2015.09.011.
[40] W. Ran, J. Jiang, X. Wang, and Z. Liu, "A multi-temporal method for detection of underground natural gas leakage using hyperspectral imaging," *Int. J. Greenhouse Gas Control*, vol. 117, no. 11, pp. 1–12, 2022, doi: 10.1016/j.ijggc.2022.103659.
[41] C. A. Rishikeshan and H. Ramesh, "An automated mathematical morphology driven algorithm for water body extraction from remotely sensed images," *ISPRS J. Photogramm. Remote Sens.*, vol. 146, pp. 11–21, 2018, doi: 10.1016/j.isprsjprs.2018.08.014.
[42] N. L. Gavankar and S. K. Ghosh, "Automatic building footprint extraction from high-resolution satellite image using mathematical morphology," *Eur. J. Remote Sens.*, vol. 51, no. 1, pp. 182–193, 2018, doi: 10.1080/22797254.2017.1416676.
[43] Y. Chen, J. P. Guerschman, Z. Cheng, and L. Guo, "Remote sensing for vegetation monitoring in carbon capture storage regions: A review," *Appl. Energy*, vol. 240, pp. 312–326, 2019.
[44] G. Lassalle, S. Fabre, A. Credoz, D. Dubucq, and A. Elger, "Monitoring oil contamination in vegetated areas with optical remote sensing: A comprehensive review," *J. Hazard. Mater.*, vol. 393, 2020, Art. no. 122427, doi: 10.1016/j.jhazmat.2020.122427.
[45] W. Ran, J. Jiang, Y. Pan, and D. Yuan, "Spectral responses and identification of surface vegetation stressed by natural gas leakage," *Int. J. Remote Sens.*, vol. 41, no. 1, pp. 132–151, 2020, doi: 10.1080/01431161.2019.1637960.
[46] Y Li et al., "Hyperspectral leaf image-based cucumber disease recognition using the extended collaborative representation model," *Sensors*, vol. 20, no. 14, 2020, Art. no. 4045, [Online]. Available: https://www.mdpi.com/774712
[47] X. Pan, J. Jiang, and D. Yuan, "A method for detecting underground natural gas pipeline micro-leakage in vegetated areas using high spatial resolution hyperspectral imagery," *Gas Sci. Eng.*, vol. 110, 2023, Art. no. 204882, doi: 10.1016/j.jgsce.2023.204882.
[48] Y. Pan, J. Jiang, Z. Liu, Y. Du, and K. Xiong, "Identification of vegetation under natural gas leakage by spectral index based on feature selection," *Int. J. Remote Sens.*, vol. 43, no. 8, pp. 3082–3105, 2022, doi: 10.1080/01431161.2022.2085068.
[49] J. B. Feret et al., "PROSPECT-4 and 5: Advances in the leaf optical properties model separating photosynthetic pigments," *Remote Sens. Environ.*, vol. 112, no. 6, pp. 3030–3043, 2008, doi: 10.1016/j.rse.2008.02.012.
[50] D. A. Sims and J. A. Gamon, "Relationships between leaf pigment content and spectral reflectance across a wide range of species, leaf structures and developmental stages," *Remote Sens. Environ.*, vol. 81, no. 2–3, pp. 337–354, 2002.
[51] G. Lassalle et al., "Detection and discrimination of various oil-contaminated soils using vegetation reflectance," *Sci. Total Environ.*, vol. 655, pp. 1113–1124, 2019, doi: 10.1016/j.scitotenv.2018.11.314.
[52] M. D. Steven, K. L. Smith, M. D. Beardsley, and J. J. Colls, "Oxygen and methane depletion in soil affected by leakage of natural gas," *Eur. J. Soil Sci.*, vol. 57, no. 6, pp. 800–807, 2006, doi: 10.1111/j.1365-2389.2005.00770.x.
[53] M. Al-Traboulsi, S. Sjögersten, J. Colls, M. Steven, and C. Black, "Potential impact of CO_2 leakage from carbon capture and storage systems on field bean (Vicia faba)," *Physiol. Plant.*, vol. 146, no. 3, pp. 261–271, 2012, doi: 10.1111/j.1399-3054.2012.01620.x.
[54] J. Hoeks, "Changes in composition of soil air near leaks in natural gas mains," *Soil Sci.*, vol. 113, no. 1, pp. 46–54, 1972.
[55] X. Wang, S. Liu, P. Du, H. Liang, J. Xia, and Y. Li, "Object-based change detection in urban areas from high spatial resolution images based on multiple features and ensemble learning," *Remote Sens.*, vol. 10, no. 2, 2018, Art. no. 276, doi: 10.3390/rs10020276.

Jinbao Jiang received the B.S. degree in engineering from the China University of Mining and Technology, Beijing, China, in 2000, and the M.S. and Ph.D. degrees in engineering from Beijing Normal University, Beijing, in 2009.

He is currently a Professor with the College of Geosciences and Surveying Engineering, China University of Mining and Technology. He teaches hyperspectral remote sensing at the undergraduate and graduate levels. His main research interests include the resources and environment remote sensing, agricultural remote sensing, and deep learning.

Yingyang Pan received the B.S. degree in geographic information system information from the Heilongjiang Institute of Technology, Harbin, China, in 2014, and the M.S. degree in civil engineering from Tianjin Chengjian University, Tianjin, China, in 2017. He is currently working toward the Ph.D. degree with the College of Geosciences and Surveying Engineering, China University of Mining and Technology, Beijing, China.

His research interests include machine learning, agricultural remote sensing, and hyperspectral image processing.

Kangning Li received the B.S. degree in geographic information system from the College of Urban and Environmental Science, Northwest University, Xi'an, China, in 2016, and the Ph.D. degree in engineering from Beijing Normal University, Beijing, China, in 2022.

She is currently a Lecturer with the College of Geosciences and Surveying Engineering, China University of Mining and Technology, Beijing. Her research interest includes agricultural remote sensing and thermal remote sensing of urban environment.

Xinda Wang received the B.S. degree in surveying and mapping engineering from the Hefei University of Technology, Hefei, China, in 2018. He is currently working toward the Ph.D. degree in photogrammetry and remote sensing with the College of Geosciences and Surveying Engineering, China University of Mining and Technology, Beijing, China.

His research interests include deep learning, agricultural remote sensing, and hyperspectral image processing.

Wenxuan Zhang received the B.S. degree in surveying and mapping engineering, in 2022, from the China University of Mining and Technology, Beijing, China, where she is currently working toward the doctoral degree in mapping science and technology.

Her research interests include hyperspectral image shadow detection and hyperspectral image processing.